Supplementary information

Magnetic-field-induced vertical alignment of carbon nanotubes in $Na_3V_2(PO_4)_2F_3$ with bulk dual-doping for high-rate sodium-ion batteries

Chen Wu [a,c,d], Yuxing Xu [a,d,*], Jiechen Song [a,c,d], Chunshan Wang [a,c,d], Qiangqiang Tan [a,b,c,d,*]

[a] *State Key Laboratory of Mesoscience and Engineering, Institute of Process Engineering, Chinese Academy of Sciences, Beijing, 100190, China*

[b] *Center of Materials Science and Optoelectronics Engineering, University of Chinese Academy of Sciences, Beijing, 100049, China*

[c] *School of Chemical Engineering, University of Chinese Academy of Sciences, Beijing, 100049, China*

[d] *Hebei Engineering Research Center of Power and Energy Storage Battery Materials, Hebei Technology Innovation Center of Advanced Energy Materials, Hebei Manufacturing Industry Innovation Center of New Energy Materials and Key Equipment, Langfang Technological Service Center of Green Industry, Langfang, 065001, China*

*** Corresponding authors:** Qiangqiang Tan, Yuxing Xu

E-mail address: qtan@ipe.ac.cn, yxxu@ipe.ac.cn

1. Supplementary Figures

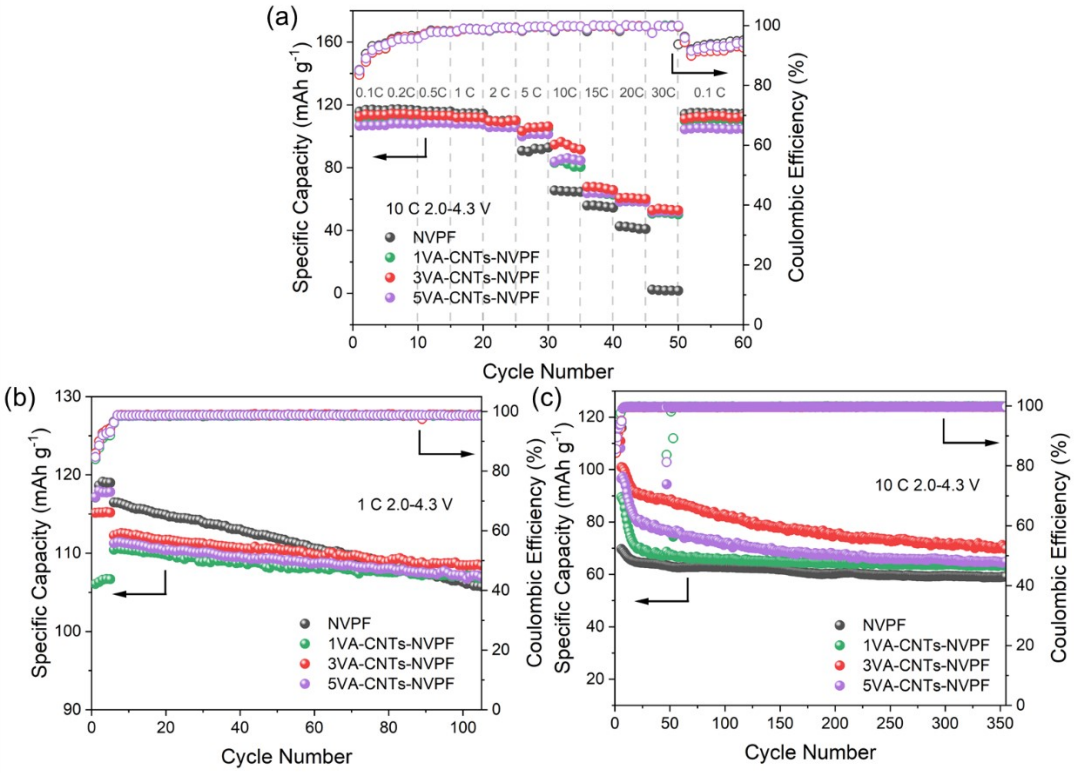

Fig. S1 (a) Rate performance of *x*VA-CNTs-NVPF cathodes (*x* = 0 wt.%, 1 wt.%, 3 wt.%, 5 wt.%). Cycling performance of *x*VA-CNTs-NVPF cathodes at (b) 1 C and (c) 10 C.

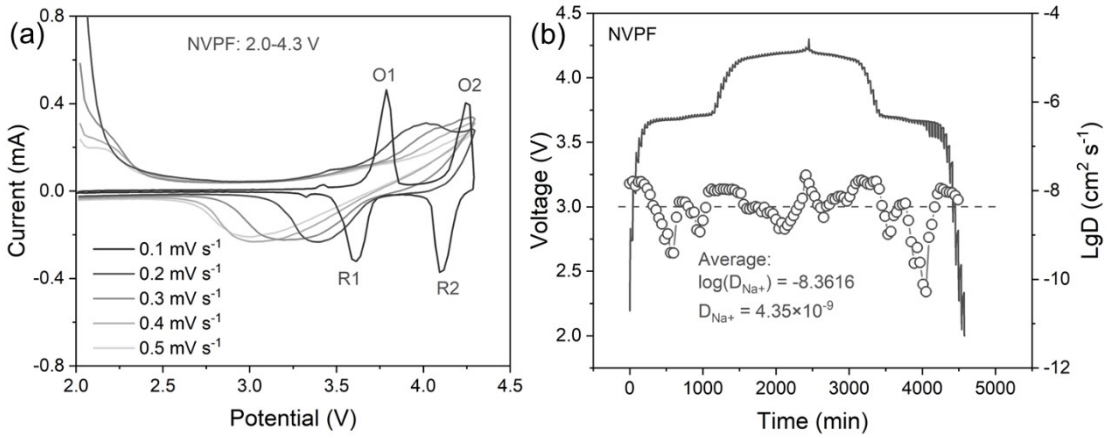

Fig. S2 (a) CV curves of NVPF cathode at various scan rates. (b) GITT test and Na^+ diffusion coefficients of NVPF cathode.

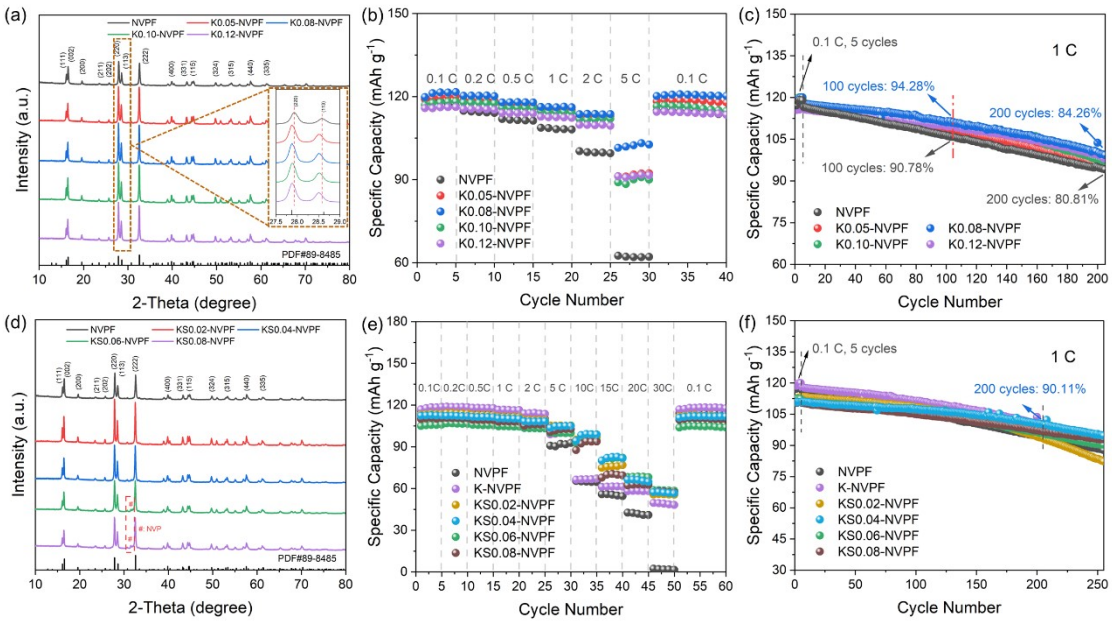

Fig. S3 (a) XRD patterns of K*x*-NVPF materials (*x* = 0, 0.05, 0.08, 0.10, 0.12). (b) Rate performance of K*x*-NVPF cathodes (*x* = 0, 0.05, 0.08, 0.10, 0.12). (c) Cycling performance of K*x*-NVPF cathodes (*x* = 0, 0.05, 0.08, 0.10, 0.12) at 1 C. (d) XRD patterns of KS*y*-NVPF materials (y = 0, 0.02, 0.04, 0.06, 0.08). (e) Rate performance of KS*y*-NVPF cathodes (y = 0, 0.02, 0.04, 0.06, 0.08). (f) Cycling performance of KS*y*-NVPF cathodes (y = 0, 0.02, 0.04, 0.06, 0.08) at 1 C.

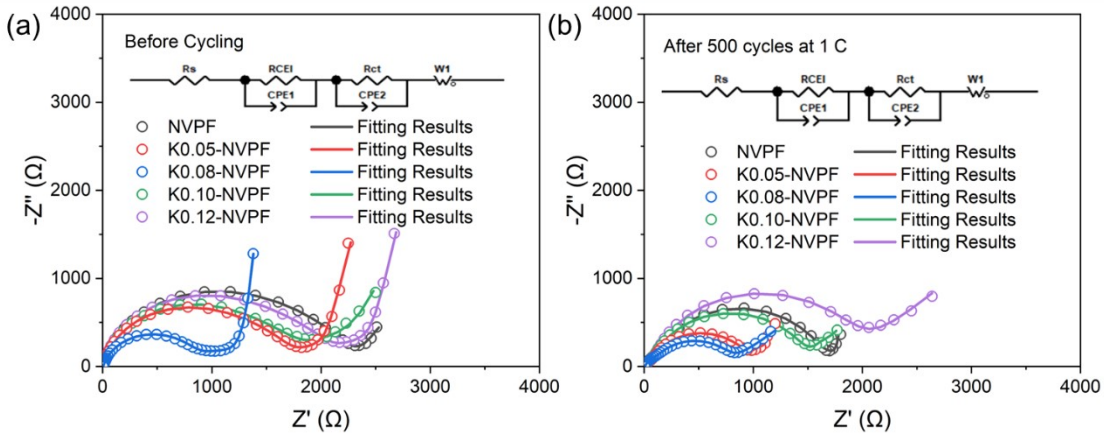

Fig. S4 The Nyquist plots and fitting equivalent of K*x*-NVPF (*x* = 0, 0.05, 0.08, 0.10, 0.12) cathodes (a) before and (b) after 500 cycles at 1 C.

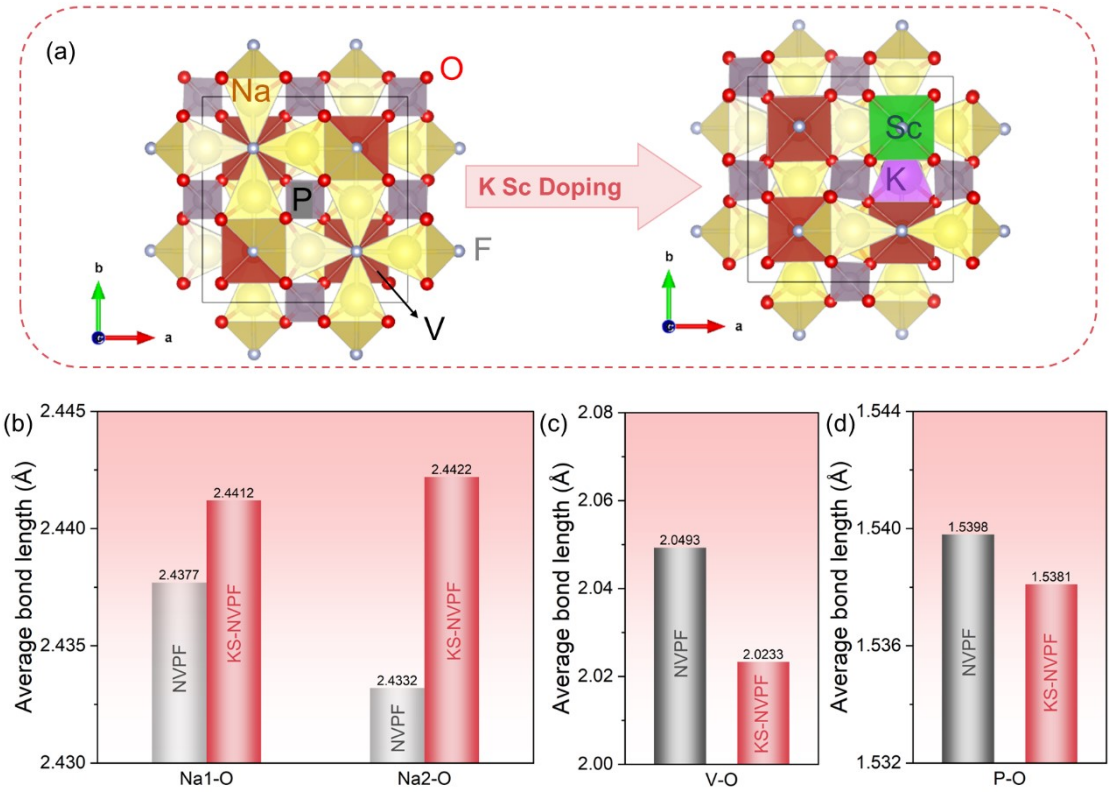

Fig. S5 (a) Structural schematic diagram of NVPF and KS-NVPF. Bond length analysis results of (b) Na-O, (c) V-O, and (d) P-O bonds of NVPF and KS-NVPF.

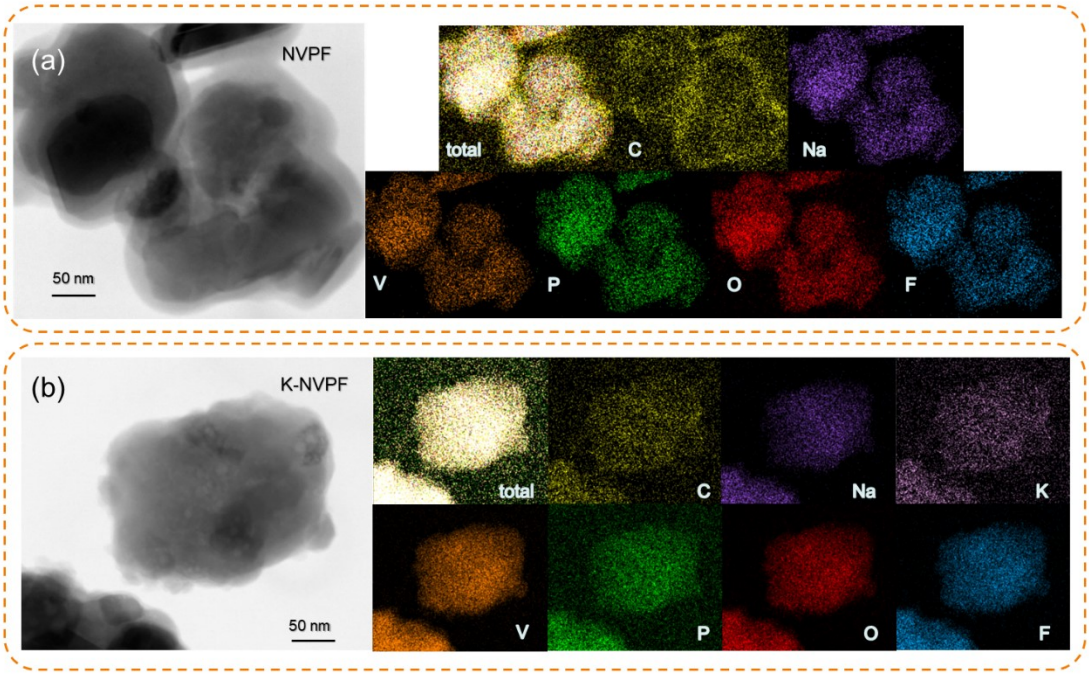

Fig. S6 EDS elemental mapping images of (a) NVPF and (b) K-NVPF.

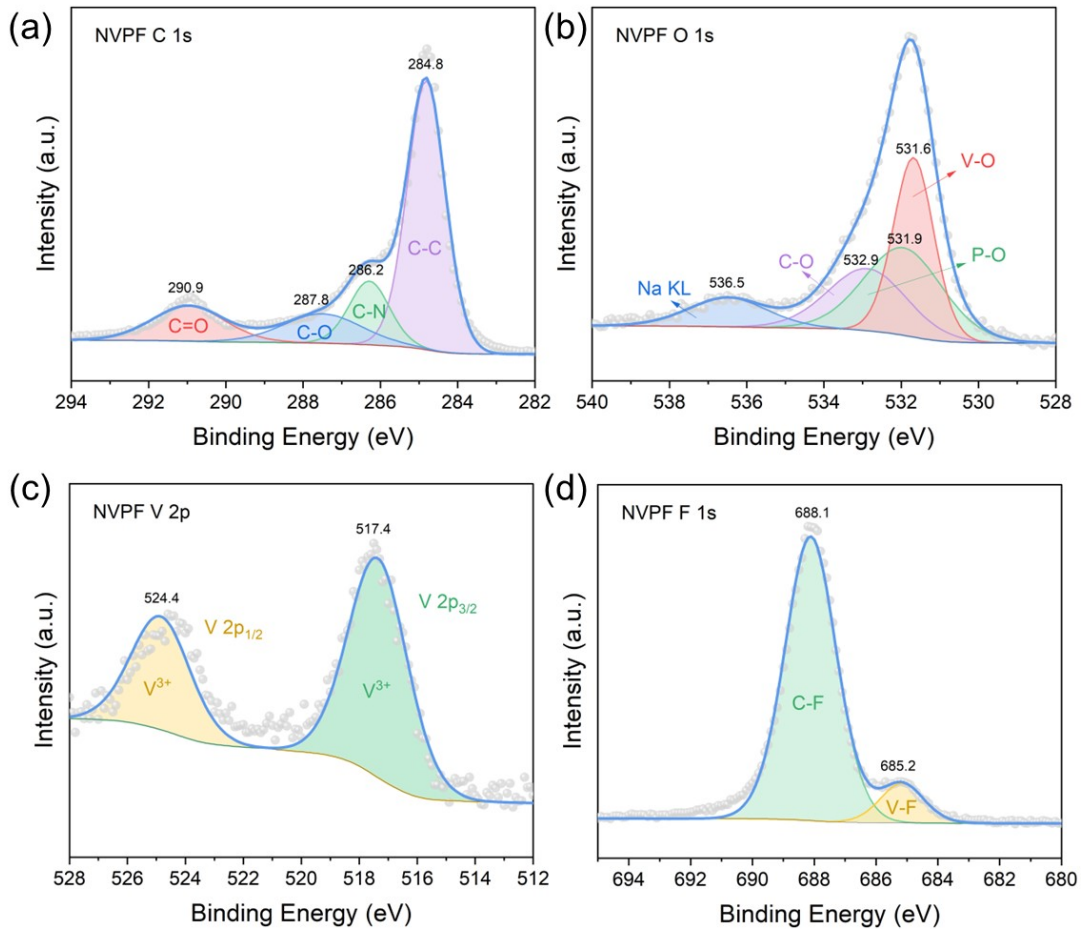

Fig. S7 XPS spectra of (a) C 1s, (b) O 1s, (c) V 2p, and (d) F 1s of the NVPF.

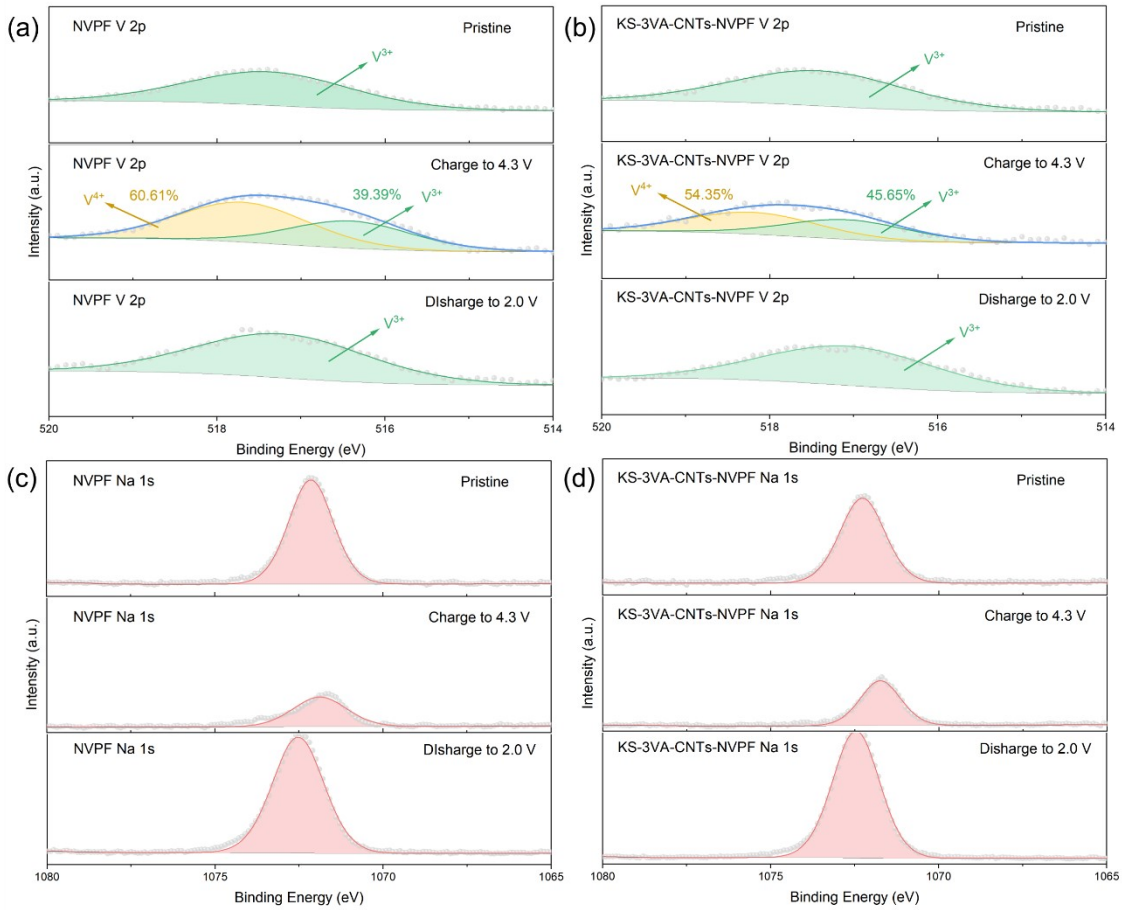

Fig. S8 Ex-situ XPS spectra of the V element at different voltages of 0.1 C of (a) NVPF and (b) KS-3VA-CNTs-NVPF cathodes. Ex-situ XPS spectra of the Na element at different voltages of 0.1 C of (c) NVPF and (d) KS-3VA-CNTs-NVPF cathodes.

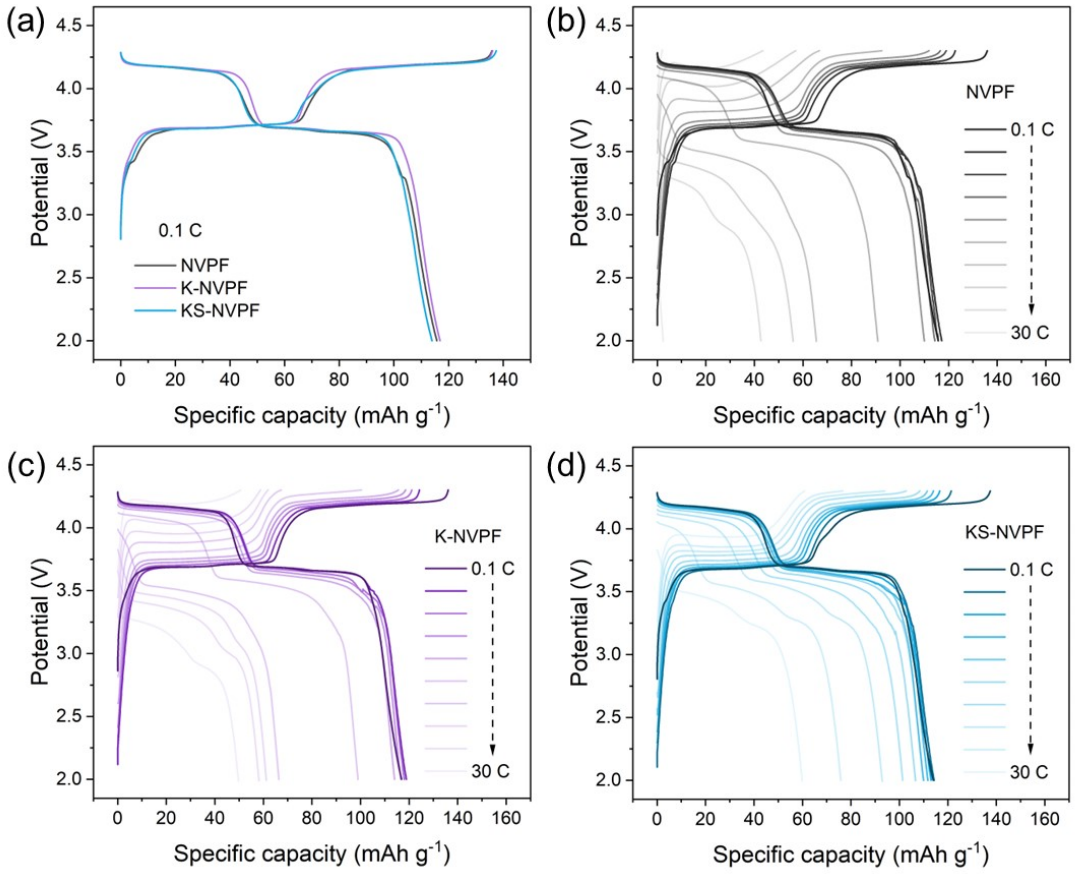

Fig. S9 (a) The charge-discharge curves of NVPF, K-NVPF, and KS-NVPF at 0.1 C. The charge-discharge curves of (b) NVPF, (c) K-NVPF, and (d) KS-NVPF from 0.1 C to 30 C.

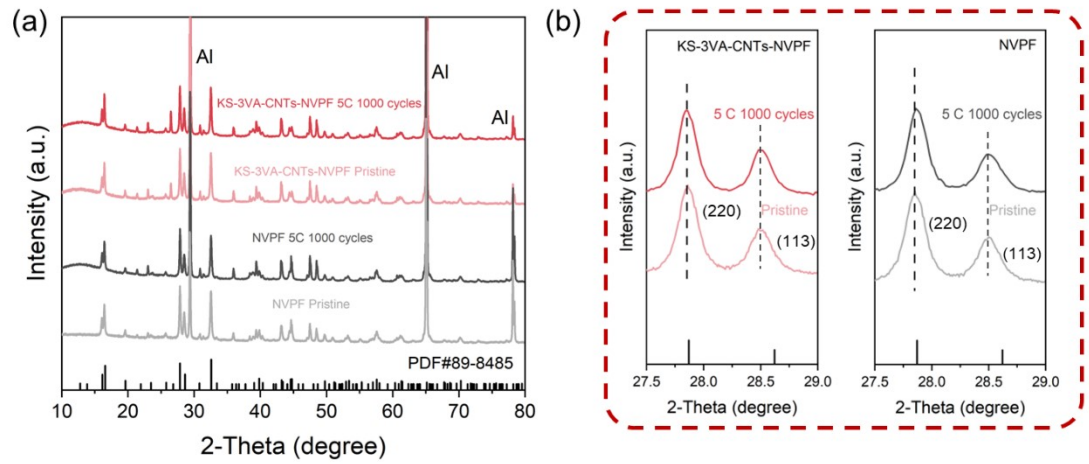

Fig. S10 (a) The XRD patterns of KS-3VA-CNTs-NVPF and NVPF before and after 1000 cycles at 5 C. (b) The enlarged patterns of the (220) and (113) peaks.

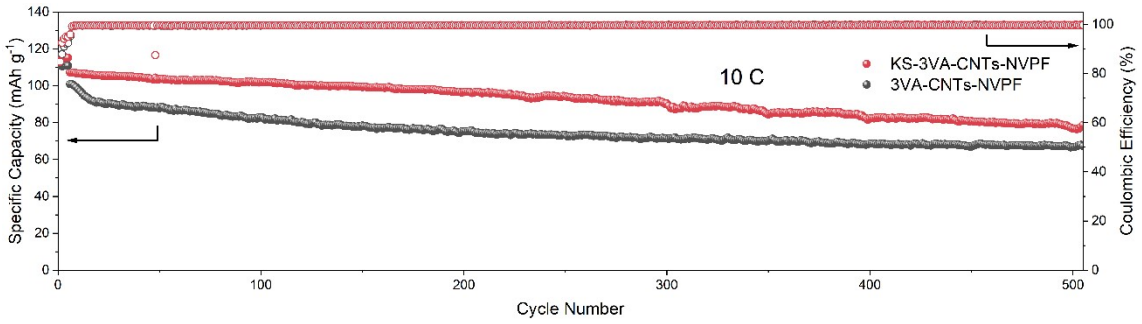

Fig. S11 Cycling performance of 3VA-CNTs-NVPF and KS-3VA-CNTs-NVPF at 10 C.

Supplementary Discussion 1: It is noteworthy that, as observed in Figs. 2a and 7a, the rate performance of 3VA-CNTs-NVPF and KS-3VA-CNTs-NVPF appears nearly identical, and both of them exhibit comparable specific capacities under extremely high current densities. This outstanding performance under high-rate conditions is primarily attributed to the critical role of the VA-CNTs conductive network in facilitating rapid electron transport and ionic diffusion, which is a common characteristic shared by the above two cathodes. However, the key contribution of K/Sc co-doping lies not in further enhancing the ultimate rate performance beyond the effect of VA-CNTs, but rather in improving the intrinsic ionic and electronic conductivity of the material (Fig. 3h and Figs. 6a-i). This ensures the structural and interfacial stability of the bulk material during high-rate cycling, thereby promoting the stable retention of high-rate performance. To further illustrate the role of K and Sc in rate enhancement, a comparison of the long-term cycling stability between KS-3VA-CNTs-NVPF and the undoped 3VA-CNTs-NVPF at 10 C reveals that although both cathodes exhibit comparable initial capacities, the undoped cathode demonstrates significantly faster capacity decay (Fig. S11). In contrast, the K/Sc co-doped cathode exhibits markedly enhanced capacity retention, indicating that K/Sc co-doping effectively improves the intrinsic ionic and electronic conductivity of the material and stabilizes the crystal structure, thereby substantially mitigating capacity degradation. This conclusion is further supported by the excellent cycling stability of KS-3VA-CNTs-NVPF at 5 C and 30 C cycling tests (Figs. 7d and e). As for the rate performance at high rate, the KS-NVPF cathode obviously delivers more stable and higher capacity at high rates than the undoped NVPF cathodes in Fig. 7a. This also confirms the key role of K and Sc in rate enhancement, which is consistent with the results of the above high-rate cycling test. Additionally, comparative electrochemical studies of NVPF, K-NVPF, and KS-NVPF materials without VA-CNTs demonstrate that the introduction of K and Sc leads to more stable cathode reaction kinetics (Figs. 6a-f), enhanced bulk ionic diffusion rates (Figs. 6g-i), and improved electronic conductivity (Fig. 3h and Figs. 7f and g). In summary, while the VA-CNTs promote rapid ion and electron transport at the electrode scale, enabling excellent rate performance in both cathodes, the K/Sc co-doping also promotes the rate enhancement of cathodes by improving the intrinsic ionic and electronic conductivity within the material. This ensures structural and interfacial stability during high-rate cycling, thereby achieving better long-term cycling stability.

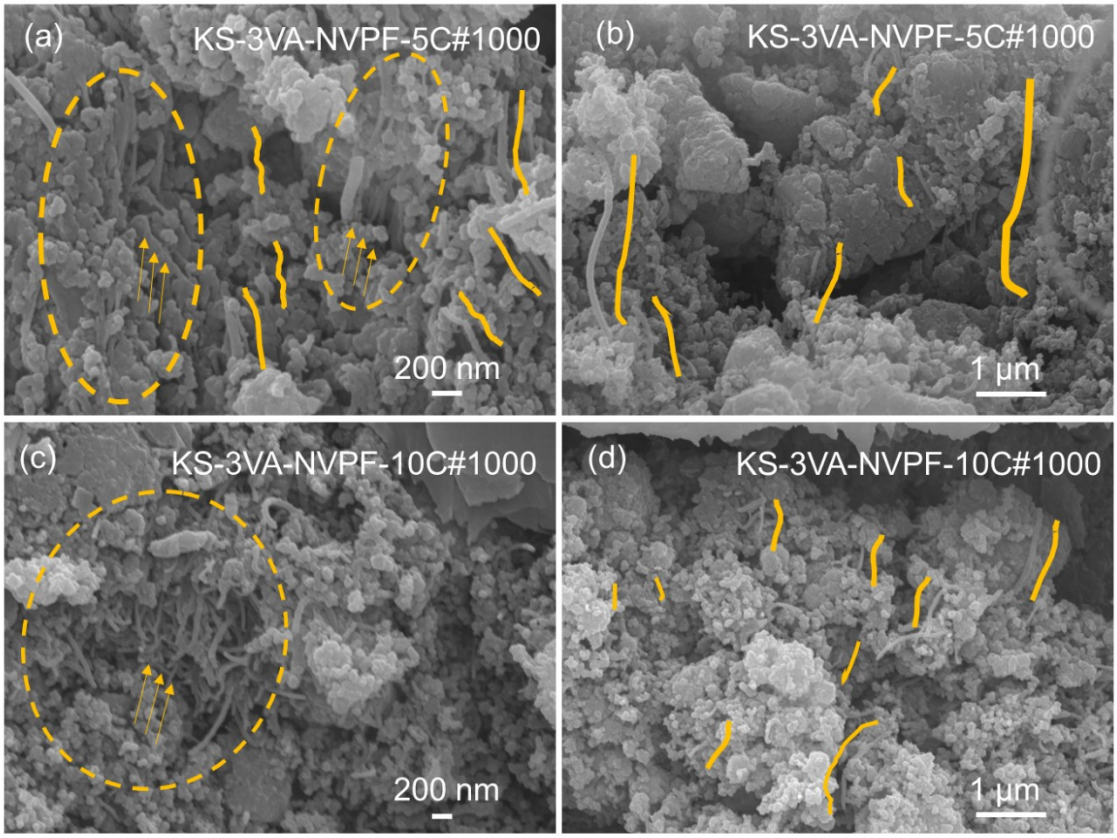

Fig. S12 SEM images of the cross section of the KS-3VA-CNTs-NVPF cathode after 1000 cycles at (a-b) 5 C and (c-d) 10 C.

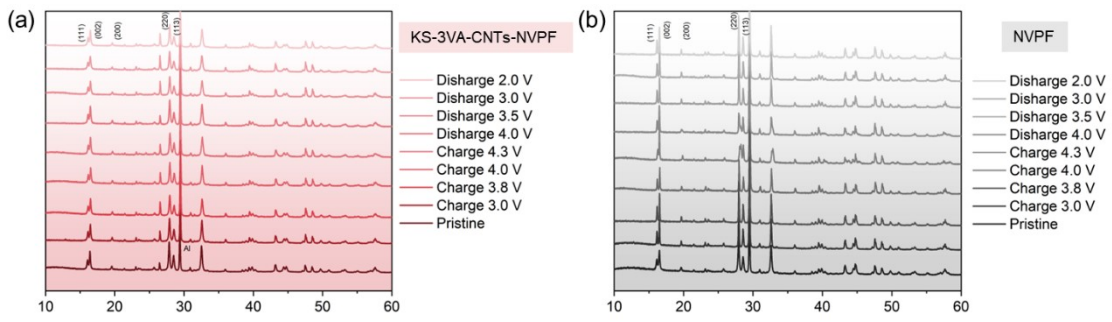

Fig. S13 The ex-situ XRD patterns of (a) KS-3VA-CNTs-NVPF and (b) NVPF cathodes during the first cycle at 0.1 C.

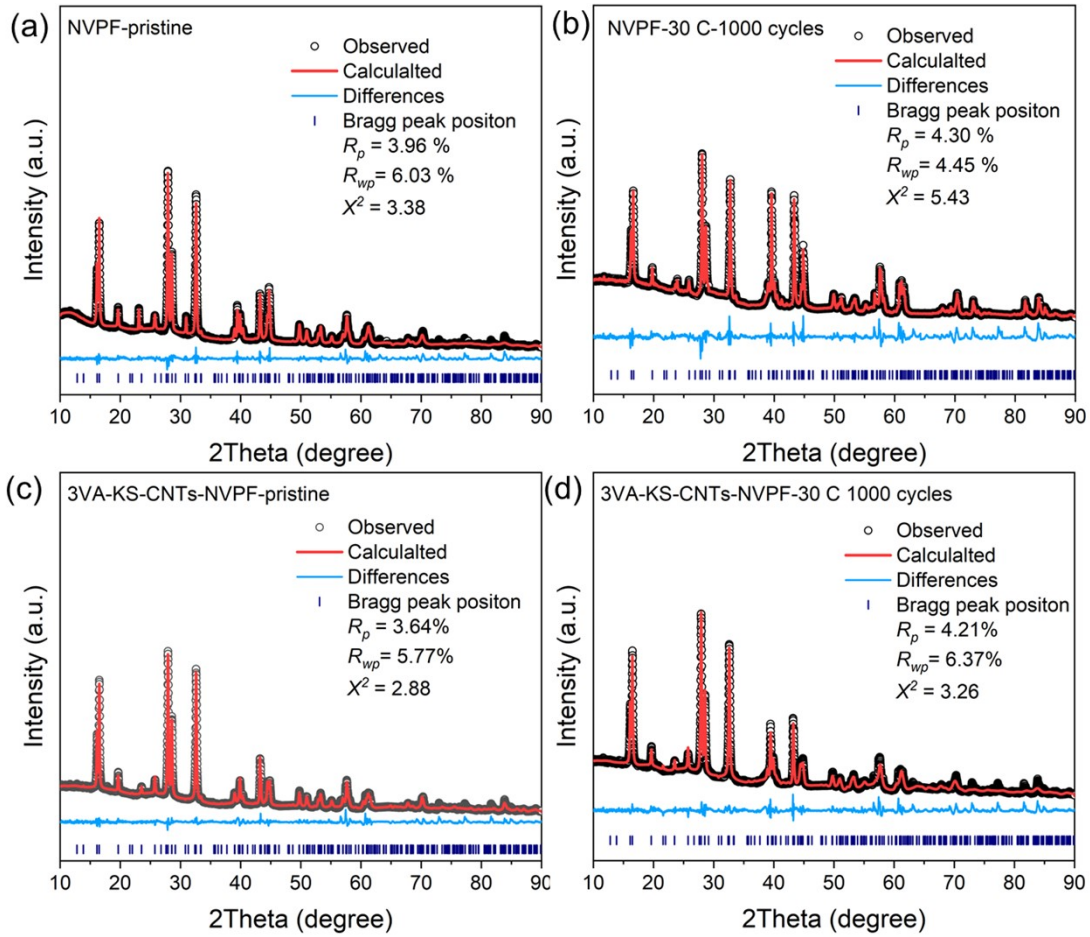

Fig. S14 Rietveld refinements of (a-b) NVPF and (c-d) KS-NVPF cathodes before and after 1000 cycles at 30 C.

2. Supplementary Tables

Table S1. EIS fitting results of the NVPF, 3R-CNTs-NVPF, and 3VA-CNTs-NVPF before cycling and after 500 cycles at 1 C.

Factor		NVPF	3R-CNTs-NVPF	3VA-CNTs-NVPF
Pristine	R_{CEI} (Ω)	1388	1225	720.8
	R_{ct} (Ω)	917.8	798.0	745.9
	R_{total} (Ω)	2309	2027	1471
After 500 cycles at 1 C	R_{CEI} (Ω)	83.47	64.04	54.63
	R_{ct} (Ω)	1503	466.6	420.5
	R_{total} (Ω)	1576	530.6	479.7

Table S2. EIS fitting results of the K*x*-NVPF (*x* = 0, 0.05, 0.08, 0.10, 0.12) before cycling and after 500 cycles at 1 C.

Factor		NVPF	K0.05-NVPF	K0.08-NVPF	K0.10-NVPF	K0.12-NVPF
Pristine	R_{CEI} (Ω)	1388	862.0	835.8	871.9	1072
	R_{ct} (Ω)	917.8	795.7	444.1	781.4	929.6
	R_{total} (Ω)	2309	1664	1285	1653	2006
After 500 cycles at 1 C	R_{CEI} (Ω)	83.47	58.44	88.49	67.64	60.06
	R_{ct} (Ω)	1503	864.5	656.2	1377	1783
	R_{total} (Ω)	1576	928.4	750.8	1450	1847

Table S3. Lattice parameters of NVPF, K-NVPF, and KS-NCPF.

Sample	a (Å)	b (Å)	c (Å)	Volume (Å^3)
NVPF	9.03586(19)	9.03586(19)	10.74617(17)	877.39(5)
K-NVPF	9.04032(8)	9.04032(8)	10.75664(10)	879.112(15)
KS-NVPF	9.03676(9)	9.03676(9)	10.74943(12)	877.831(18)

Table S4. Refined structural parameters of NVPF, K-NVPF, and KS-NVPF.

Sample	Atom	Site	x	y	z	Occupancy	Uiso
NVPF	Na1	8i	0.52816	0.23128	0.00000	1.00000	0.02530
	Na2	8i	0.81900	0.07509	0.00000	0.50000	0.04390
	V1	8j	0.25006	0.25006	0.18646	1.00000	0.00690
	P1	4d	0.00000	0.50000	0.25000	1.00000	0.00080
	P2	4e	0.00000	0.00000	0.26032	1.00000	0.02920
	O1	16k	0.09295	0.40076	0.16210	1.00000	0.01580
	O2	8j	0.09142	0.09142	0.16477	1.00000	0.00310
	O3	8j	0.39930	0.39930	0.16220	1.00000	0.00090
	F1	4f	0.23456	0.23456	0.00000	1.00000	0.01990
	F2	8j	0.24674	0.24674	0.36542	1.00000	0.01360
K-NVPF	Na1	8i	0.52471	0.22792	0.00000	0.96500	0.03070
	Na2	8i	0.80925	0.06398	0.00000	0.48500	0.04490
	K1	8i	0.52471	0.22792	0.00000	0.03500	0.03070
	K2	8i	0.80925	0.00000	0.00000	0.01500	0.04490
	V1	8j	0.25081	0.25081	0.18639	1.00000	0.00990
	P1	4d	0.00000	0.50000	0.25000	1.00000	0.01000
	P2	4e	0.00000	0.00000	0.26068	1.00000	0.01960
	O1	16k	0.09695	0.39873	0.16514	1.00000	0.01910
	O2	8j	0.08709	0.08709	0.16597	1.00000	0.00460
	O3	8j	0.40350	0.40350	0.15982	1.00000	0.00020
	F1	4f	0.23692	0.23692	0.00000	1.00000	0.01850
	F2	8j	0.24575	0.24575	0.36443	1.00000	0.00610
KS-NVPF	Na1	8i	0.52701	0.23508	0.00000	0.96390	0.02970
	Na2	8i	0.82256	0.09064	0.00000	0.48610	0.05660
	K1	8i	0.52701	0.23508	0.00000	0.03610	0.02970
	K2	8i	0.82256	0.09064	0.00000	0.01390	0.05660
	V1	8j	0.24872	0.24872	0.18635	0.98190	0.00950
	Sc	8j	0.24872	0.24872	0.18635	0.01810	0.00950
	P1	4d	0.00000	0.50000	0.25000	1.00000	0.04260
	P2	4e	0.00000	0.00000	0.25256	1.00000	0.00760
	O1	16k	0.09338	0.40054	0.16306	1.00000	0.00340
	O2	8j	0.09012	0.09012	0.16068	1.00000	0.02760
	O3	8j	0.40082	0.40082	0.15985	1.00000	0.00730
	F1	4f	0.23770	0.23770	0.00000	1.00000	0.01570
	F2	8j	0.24171	0.24171	0.36575	1.00000	0.02190

Table S5. EIS fitting results of the NVPF, K-NVPF, KS-NVPF, and KS-3VA-CNTs-NVPF before cycling and after 500 cycles at 1 C.

Factor		NVPF	K-NVPF	KS-NVPF	KS-3VA-CNTs-NVPF
Pristine	R_{CEI} (Ω)	1388	835.8	687.7	530.4
	R_{ct} (Ω)	917.8	444.1	326.6	127.5
	R_{total} (Ω)	2309	1285	1018	662.5
After 500 cycles at 1 C	R_{CEI} (Ω)	83.47	88.49	23.04	8.082
	R_{ct} (Ω)	1503	656.2	462.9	222.0
	R_{total} (Ω)	1576	750.8	490.6	234.2

Supplementary Discussion 2: It is worth noting that the "contradiction" between the relatively large total impedance value of the battery under initial conditions and its satisfactory high-rate performance can be explained by the following reasons:

As can be observed from Fig. 7f and Table S5, the large impedance observed in the Nyquist plots of various materials before cycling is primarily attributed to the interfacial resistance (R_{CEI}). This is because the cathode-electrolyte interphase (CEI) layer on the cathode surface is not yet stabilized during the initial cycles, and its unstable structural change leads to a higher R_{CEI}. This resistance dominates in the intermediate frequency range typically measured by EIS, which reflects the energy barrier for Na^+ immigration across the electrode-electrolyte interface under near-equilibrium conditions in the initial state. [1, 2] However, the interface resistance is no longer the dominant element when cycling at high rates. Specifically, electrode reactions under high-rate cycling are generally non-equilibrium processes with increased polarization. Under such conditions, the driving force (overpotential) is relatively high. Therefore, although the interfacial resistance R_{CEI} exists, the charge transfer resistance (R_{ct}) reflecting electrode reactions is actually the dominant element in this situation. [3, 4] For the KS-3VA-CNTs-NVPF material, the R_{ct} before cycling is 127.5 Ω, which is competitive compared to other similar materials, [3-11] and it only increases to 222.0 Ω after 500 cycles at 1 C, exhibiting high ionic and electronic transport abilities within the cathode. These bulk material characteristics can further enable sodium ions and electrons to be transported rapidly once the stable CEI layer is established (Fig. 7g and Table S5), allowing the cathode to exhibit satisfactory high-rate performance (Figs. 7a, 7d-e).

Therefore, this seemingly "contradictory" phenomenon arises because the EIS test sensitively captures the interfacial-limited kinetics of the battery under equilibrium conditions in the initial state, whereas the high-rate performance of KS-3VA-CNTs-NVPF is collectively determined by the rapid bulk transport kinetics under high-polarization conditions and the stabilization of the CEI layer after cycling.

Table S6. Electrochemical performance of the KS-3VA-CNTs-NVPF cathode compared to that of other related cathodes.

Cathode materials	Modification measures	Rate performance	Capacity retention (%)	Ref.
NVPF-Mg05	Mg	10 C: 96.6 mAh g^{-1}	69.4 (1000 cycles, 10 C)	9
Fe0.1-NVPF@ N-CNTs	Fe, CNTs	10 C: 35 mAh g^{-1}	74.53 (1000 cycles, 2 C)	4
NVPF@NC-Cu0.06	Cu, N-C	10 C: 99 mAh g^{-1}	94 (500 cycles, 10 C)	5
NVPF@N-3	N-C	10 C: 102.6 mAh g^{-1}	96.5 (100 cycles, 1 C)	12
NVMPF	Fe, Ni, Co, Mg, Cr	10 C: 114 mAh g^{-1}	94.6 (200 cycles, 10 C)	13
K0.10-NVPF	K	10 C: 90.6 mAh g^{-1}	97.5 (500 cycles, 1 C)	6
NVPF@C@CMC-2	CMC	10 C: 83.2 mAh g^{-1}	74 (500 cycles, 10 C)	10
KS-3VA-CNTs-NVPF	K, Sc, VA-CNTs	**10 C: 100.1 mAh g^{-1}**	**90.33** (500 cycles, 5 C) **75.94** (1000 cycles, 30 C)	(This work)

Table S7. Summary of data on the lattice parameters of NVPF and KS-3VA-CNTs-NVPF cathodes before and after 1000 cycles at 30 C obtained by XRD Rietveld refinement.

Sample	a (Å)	b (Å)	c (Å)	Volume (Å^3)
NVPF-pristine	9.0376(7)	9.0376(7)	10.7449(5)	877.62(16)
NVPF-30 C	9.0005(10)	9.0005(10)	10.6720 (6)	864.52 (14)
KS-3VA-CNTs-NVPF-pristine	9.0419(5)	9.0419(5)	10.7490(4)	878.80(12)
KS-3VA-CNTs-NVPF-30 C	9.0391(13)	9.0391(13)	10.7567(10)	878.88(31)

References

1. A. Chahbaz, M. Schreiber, J. Rinner, J. M. Hinojosa, G. Stahl, M. Lienkamp and D. U. Sauer, *Cell Rep. Phys. Sci.*, 2025, **6**, 102654.
2. W. Waag, S. Käbitz and D. U. Sauer, *Appl. Energy*, 2013, **102**, 885-897.
3. S. Guo, J. Peng, N. Sharma, J. Pan, Y. Liao, X. An, H. Li, Z. Ge, C. Zhou, W. L. Tan and J. Liu, *Chem. Mater.*, 2025, **37**, 1500-1512.
4. J. Yang, N. Liu, G. Jiang, W. Sheng, X. Zheng, Z. Bai and X. Jiang, *Chem. Eng. J.*, 2024, **485**, 149834.
5. Q. Zhou, Y. Wang, R. Ou, X. Ding, Y. Xin, F. Wu and H. Gao, *Small*, 2024, **20**, 2310699.
6. J. Zhang, Y. Lai, P. Li, Y. Wang, F. Zhong, X. Feng, W. Chen, J. Liu, X. Ai, H. Yang and Y. Cao, *Green Energy Environ.*, 2022, **7**, 1253-1262.
7. B. Wang, J. Zhang, Y. Zhao, M. Zhang, L. Guo and Y. Chen, *Energy Storage Mater.*, 2025, **82**, 104661.
8. D. A. Puspitasari, J. Patra, I. M. Hung, D. Bresser, T.-C. Lee and J.-K. Chang, *ACS Sustainable Chem. Eng.*, 2021, **9**, 6962-6971.
9. Y. Zhang, Y. Hu, T. Feng, Z. Xu and M. Wu, *J. Power Sources*, 2024, **602**, 234337.
10. K. Liang, H. Zhao, J. Li, X. Huang and Y. Ren, *Appl. Surf. Sci.*, 2023, **615**, 156412.
11. X. Wang, Q. Wang, J. Zhang, Y. Ma, M. Huang and X. Liu, *J. Energy Chem.*,

2025, **102**, 365-376.

12. G.-d. Yi, C.-l. Fan, Z. Hu, W.-h. Zhang, S.-c. Han and J.-s. Liu, *Electrochim. Acta*, 2021, **383**, 138370.

13. M. Sun, Y. Sun, H. Ma, S. Wang, Q. Liu, G. Zhao, L. Duan, Q. Hu, Q. An, K. Zeng, W. Huang, X. Zou, Y. Yang and H. Guo, *ACS Nano*, 2025, **19**, 18386-18396.